



# THE INFLUENCE OF DENSE GAS RINGS ON THE DYNAMICS OF A STELLAR DISK IN THE GALACTIC CENTER

ALESSANDRO A. TRANI<sup>1,2</sup>, MICHELA MAPELLI<sup>2</sup>, ALESSANDRO BRESSAN<sup>1,2</sup>, FEDERICO I. PELUPESSY<sup>3,4</sup>, ARJEN VAN ELTEREN<sup>3</sup>, AND SIMON PORTEGIES ZWART<sup>3</sup>

<sup>1</sup> Scuola Internazionale Superiore di Studi Avanzati (SISSA), Via Bonomea 265, I-34136, Trieste, Italy; [aatrani@gmail.com](mailto:aatrani@gmail.com)

<sup>2</sup> INAF-Osservatorio Astronomico di Padova, Vicolo dell'Osservatorio 5, I-35122, Padova, Italy

<sup>3</sup> Leiden Observatory, Leiden University, P.O. Box 9513, NL-2300 RA, Leiden, The Netherlands

<sup>4</sup> Institute for Marine and Atmospheric Research Utrecht, Department of Physics and Astronomy Utrecht, University Princetonplein 5, 3584 CC Utrecht, The Netherlands

Received 2015 September 17; accepted 2015 December 8; published 2016 February 4

## ABSTRACT

The Galactic center hosts several hundred early-type stars, about 20% of which lie in the so-called clockwise disk, while the remaining 80% do not belong to any disks. The circumnuclear ring (CNR), a ring of molecular gas that orbits the supermassive black hole (SMBH) with a radius of  $\sim 1.5$  pc, has been claimed to induce precession and Kozai–Lidov oscillations onto the orbits of stars in the innermost parsec. We investigate the perturbations exerted by a gas ring on a nearly Keplerian stellar disk orbiting an SMBH by means of combined direct  $N$ -body and smoothed particle hydrodynamics simulations. We simulate the formation of gas rings through the infall and disruption of a molecular gas cloud, adopting different inclinations between the infalling gas cloud and the stellar disk. We find that a CNR-like ring is not efficient in affecting the stellar disk on a timescale of 3 Myr. In contrast, a gas ring in the innermost 0.5 pc induces precession of the longitude of the ascending node  $\Omega$ , which significantly affects the stellar disk inclination. Furthermore, the combined effect of two-body relaxation and  $\Omega$ -precession drives the stellar disk dismembering, displacing the stars from the disk. The impact of precession on the star orbits is stronger when the stellar disk and the inner gas ring are nearly coplanar. We speculate that the warm gas in the inner cavity might have played a major role in the evolution of the clockwise disk.

*Key words:* black hole physics – Galaxy: center – ISM: clouds – methods: numerical – stars: kinematics and dynamics

## 1. INTRODUCTION

Several hundred young early-type stars lie in the vicinity of SgrA\*, the compact radio source associated with the supermassive black hole (SMBH) at the center of our Galaxy (Krabbe et al. 1991, 1995; Morris 1993; Genzel et al. 2003; Ghez et al. 2003, 2005; Schödel et al. 2003; Eisenhauer et al. 2005; Paumard et al. 2006; Gillessen et al. 2009). Some of these stars lie in a nearly Keplerian disk, called the clockwise (CW) disk because of the motion that it shows when projected on the plane of the sky (Paumard et al. 2006; Bartko et al. 2009; Lu et al. 2009, 2013; Do et al. 2013; Yelda et al. 2014). Bartko et al. (2009) suggest that the CW disk extends up to 0.5 pc and is warped or tilted because the orientation of its normal axis changes by  $60^\circ$  from the inner edge to the outer edge. Furthermore, Bartko et al. (2009) suggest the presence of a second dissolving counterclockwise disk. However, recent results from Yelda et al. (2014) show that the CW disk extends only up to 0.13 pc and it is neither significantly warped nor tilted. Moreover, Yelda et al. (2014) find no evidence of counterclockwise motion and estimate that only  $\sim 20\%$  of the O and Wolf–Rayet stars lie in the CW disk.

The origin of the young stars is puzzling: the tidal shear from the SMBH should disrupt nearby molecular clouds and prevent star formation. However, a disrupted molecular cloud might settle into a disk around the SMBH, which could fragment and form stars (Bonnell & Rice 2008; Mapelli et al. 2008, 2012, 2013; Hobbs & Nayakshin 2009; Alig et al. 2011, 2013; Lucas et al. 2013; Jalali et al. 2014; Mapelli & Ripamonti 2015; see Mapelli & Gualandris 2016 for a recent review). This scenario can reproduce the observational features of the CW disk but

cannot explain the young stars that do not lie within the disk. A possible scenario to explain such stars is to invoke precession effects that perturb and dismember the CW disk.

The SMBH and the young stars are embedded into the cusp of the nuclear star cluster, which has a nearly spherical density profile (Genzel et al. 2003; Schödel et al. 2007) and is a source of mass precession and two-body relaxation (Löckmann et al. 2009). The circumnuclear ring (CNR), a ring of molecular gas that orbits the SMBH with a radius of  $\sim 1.5$  pc, might also perturb the CW disk. In particular, the nearly axisymmetric potential of the CNR might induce precession of the mean orbital elements of a stellar orbit, specifically inclination  $i$ , eccentricity  $e$ , argument of periapsis  $\omega$ , and longitude of the ascending node  $\Omega$  (Šubr et al. 2009; Ulubay-Siddiki et al. 2009; Haas et al. 2011a, 2011b; Šubr & Haas 2012; Mapelli et al. 2013). If the plane of the orbit and the plane of the axisymmetric potential are misaligned, periodic oscillations in inclination and eccentricity appear. These oscillations, called Kozai–Lidov cycles (Kozai 1962; Lidov 1962), might be suppressed by the presence of a strong spherical potential such as the stellar cusp (Ivanov et al. 2005; Chang 2009; Löckmann et al. 2009; Šubr et al. 2009). While these dynamical processes have been investigated for a long time, there is still debate on the actual importance of Kozai–Lidov and precession effects. In particular, the interplay between the CNR and the stellar cusp is still unclear, and previous studies neglected the influence of gas lying in the inner cavity (i.e., inside the CNR).

Our aim is to investigate the precession induced by dense gaseous rings on the CW disk. We generate such rings self-consistently by simulating the disruption of a turbulence-supported molecular cloud. In this way, we obtain rings that

match the main properties of the CNR and we also account for the presence of warm gas in the inner cavity (Mapelli & Trani 2015). We investigate precession effects by means of a direct-summation  $N$ -body code coupled with a smoothed particle hydrodynamics (SPH) code thanks to the AMUSE software environment (Portegies Zwart et al. 2009, 2013; Pelupessy et al. 2013). In particular, we study the dependence of precession on the angle between the CW disk and a gas ring. We show that the warm gas that lies in the inner cavity might substantially affect the evolution of the young stars in the Galactic center (GC). In Section 2 we describe the methodology we employed for our simulations; in Section 3 we present our results. In Section 4 we discuss the implications of our work and compare it with previous results. Our conclusions are presented in Section 5.

## 2. METHODS

We use the AMUSE software environment (Portegies Zwart et al. 2009, 2013; Pelupessy et al. 2013) to combine different gas and stellar physics in a single simulation. AMUSE is a Python framework that embeds several codes that are specialized solvers in a single physics domain—stellar evolution, gravitational dynamics, hydrodynamics, and radiative transfer. One of the main features of AMUSE is its ability to couple and run different codes in a single simulation. In particular, it enables the gravitational coupling between the particles of different codes through BRIDGE (Fujii et al. 2007), which is an extension of the mixed-variable symplectic scheme from Holman & Wisdom (1991).

We use the  $N$ -body SPH code GASOLINE (Wadsley et al. 2004; Read et al. 2010) to simulate the formation of a CNR-like gas ring through the infall and disruption of a molecular gas cloud. The molecular cloud is simulated as in run r1 of Mapelli & Trani (2015), who investigate the formation of circumnuclear disks. In particular, the molecular cloud is modeled as a spherical cloud with a radius of 15 pc and a total mass of  $1.3 \times 10^5 M_\odot$ . Each gas particle has a mass of  $1.2 M_\odot$ . It has an impact parameter of  $b = 26$  pc and an initial velocity of  $v_{\text{in}} = 0.208 v_{\text{esc}}$ , where  $v_{\text{esc}}$  is the escape velocity from the SMBH at 25 pc. The cloud is seeded with supersonic turbulent velocities and is marginally self-bound (see Hayfield et al. 2011). We include radiative cooling, using the same prescriptions as in Mapelli et al. (2012).

GASOLINE uses a kick-drift-kick scheme to integrate the evolution of particles. This scheme is second-order accurate in positions and velocities. To achieve higher accuracy in integrating stellar orbits, we calculate the stellar dynamics of a thin stellar disk using the fourth-order Hermite  $N$ -body code PhiGRAPE and couple this with the time-evolving potential generated by the snapshots of the SPH simulation using a fourth-order BRIDGE scheme (G. Ferrari et al. 2015, in preparation). The assumption here is that the evolution of the thin stellar disk does not affect the evolution of the gas disk, which is justified by the low mass of the stellar disk compared with the other mass components ( $\approx 3\%$ ).

To achieve higher accuracy in integrating stellar orbits, we calculate the stellar dynamics of a thin stellar disk using the direct  $N$ -body code PhiGRAPE (Harfst et al. 2007) and couple this with the time-evolving potential generated by the snapshots of the SPH simulation using a fourth-order BRIDGE scheme (G. Ferrari et al. 2015, in preparation). The assumption here is that the evolution of the thin stellar disk does not affect the

evolution of the gas disk, which is justified by the low mass of the stellar disk compared with the other mass components ( $\approx 3\%$ ). PhiGRAPE uses a fourth-order Hermite predictor-corrector scheme to integrate the evolution of the stars. We run PhiGRAPE on GPUs through the SAPPORO library (Gaburov et al. 2009). We modified both PhiGRAPE and GASOLINE to include the potential of the SMBH and of the stellar cusp. The SMBH is modeled as a point-mass potential with a mass of  $M_{\text{SMBH}} = 3.5 \times 10^6 M_\odot$  (Ghez et al. 2003). The stellar cusp is modeled as a rigid potential given by a spherical distribution of mass whose mass density follows the broken-law profile of Schödel et al. (2007):

$$\rho(r) = 2.8 \times 10^6 M_\odot \text{pc}^{-3} \left(\frac{r}{r_0}\right)^{-\gamma}, \quad (1)$$

with  $r_0 = 0.22$  pc,  $\gamma = 1.75$  for  $r > r_0$ , and  $\gamma = 1.2$  for  $r < r_0$ .

For the disk of stars we adopt the outcome of run E<sup>5</sup> of Mapelli et al. (2012). In particular, the stellar disk we simulate is composed of 1252 stars with an initial mass function given by a power law with an index of  $\alpha = 1.5$  and a lower mass limit of  $1.3 M_\odot$ . The total mass of the disk is  $4.3 \times 10^3 M_\odot$ , which is lower than suggested by the most recent observations of the young stars in the central parsec ( $\sim(5\text{--}20) \times 10^3 M_\odot$  according to Lu et al. 2013). However, we prefer using a set of stellar orbits that formed self-consistently (from the simulation by Mapelli et al. 2012) rather than drawing stellar orbits with Monte Carlo sampling.

The stars have semimajor axis  $a$  ranging from 0.1 to 0.4 pc and mean eccentricity  $\langle e \rangle = 0.3$  (the eccentricity distribution is in excellent agreement with the data reported by Yelda et al. 2014). The disk has an initial opening angle of  $\sim 7^\circ$ .

We simulate different inclinations  $\theta_i$  between the infalling gas cloud and the stellar disk. To do this, we simply rotate the snapshots of the SPH simulation with respect to the plane of the stellar disk. We choose three different inclinations:  $\theta_i = 10^\circ$  (run A),  $45^\circ$  (run B), and  $90^\circ$  (run C). The secular evolution of the orbital elements of a star in an axisymmetric potential strongly depends on the inclination between the orbital plane and the symmetry axis; therefore, we expect different outcomes for different inclinations. To compare our results, we also integrate the evolution of the stellar disk alone without any infalling molecular gas cloud (run D). Table 1 shows a summary of the runs presented in this paper.

We stop the simulations at 3 Myr because this is the best observational estimate for the age of the young stars in the central parsec (Lu et al. 2013). Furthermore, after this time, stellar mass changes and the energy input from supernovae and stellar winds become progressively more important.

<sup>5</sup> This procedure is not completely self-consistent because we take the initial conditions for the stellar disk from another simulation instead of forming the young stars and the gas rings in the same simulation. However, integrating the formation of the stars and studying the dynamical influence of gas rings in the same simulation is computationally prohibitive. In fact, run E of Mapelli et al. (2012) has a factor of 30 higher resolution with respect to the simulations that will be discussed in this paper. Such high resolution is necessary to follow the first stages of the fragmentation process with sufficient accuracy, but run E of Mapelli et al. (2012) stalls after  $\sim 5 \times 10^5$  yr. In contrast, to investigate the dynamical effects of gas onto the stellar orbits, we can adopt a lower resolution for the gas component, while we need a much higher accuracy in the integration of stellar dynamics (therefore, we use PhiGRAPE).

**Table 1**  
Main Properties of the Simulations

Run	Perturber	$\theta_i$	$\theta_{\text{inner}}$	Notes
A	Yes	10	20	...
B	Yes	45	37	...
C	Yes	90	77	...
D	No	...	...	...
A0	Yes	10	20	No outer ring
A1	Yes	10	20	Massless stars

**Note.** Column 1: run name; column 2: presence of a perturber (i.e., a molecular cloud falling toward the SMBH); column 3: initial inclination  $\theta_i$  between the molecular cloud and the stellar disk; and column 4: average inclination  $\theta_{\text{inner}}$  between the stellar disk and the inner ( $r \sim 0.2\text{--}0.4$  pc) gas ring.

### 3. RESULTS

In the first 1 Myr, the gas cloud quickly inspirals toward the SMBH and settles down into a disk. Figure 1 shows the projected density map of the gas ring seen face-on (top panel) and edge-on (bottom panel) at 1 Myr in run A. The formation of the gas ring is similar to the one described in Section 3.1 of Mapelli et al. (2013). At 0.2 Myr, the cloud is completely disrupted into several streamers. At 0.5 Myr, the streamers begin to form a ring around the SMBH. This ring is progressively formed as the inspiraling streamers settle down around the SMBH. At 1.2 Myr, each gas streamer has settled down and the gas ring is completely formed. The gas ring is actually composed of two concentric rings. The outer ring is composed of irregular and clumpy gas streamers and has an inner radius of  $\sim 1.5$  pc. The inner ring is warped and has a radius of  $\sim 0.2\text{--}0.4$  pc, similar to the stellar disk. The inner gas ring has a mass of  $\sim 3 \times 10^3 M_\odot$ , while the outer ring has a mass of  $\sim 9 \times 10^4 M_\odot$ . In addition, the inner ring is inclined by  $\sim 24^\circ$  with respect to the outer ring; hence, the stellar disk and the inner gas ring have a mutual inclination  $\theta_{\text{inner}}$  (see Table 1). This misalignment is due to the fact that the inner ring comes from low impact parameter and low angular momentum gas that engulfs the SMBH during the first periapsis passage of the cloud, while the outer ring forms later during the subsequent periapsis passages of the disrupted cloud (and suffers from gravitational focusing and torques). A detailed explanation is given in Mapelli & Trani (2015).

Once the gas ring has settled, it induces precession on the stellar disk and alters the stellar orbits. The evolution of eccentricity and semimajor-axis distributions is similar in each run, both those including the infalling gas cloud (runs A, B, and C) and those that do not include gas (run D). In particular, after  $\sim 1.5$  Myr the eccentricity distribution becomes bimodal, showing two peaks at  $e \sim 0.15$  and  $0.5$  (Figure 2, top panel).

The semimajor axis distribution does not change significantly throughout the simulations (Figure 2, bottom panel) and indicates that in our model, two-body relaxation of orbital energy is inefficient. This result is in agreement with Šubr & Haas (2014), who find that two-body relaxation is inefficient in changing the semimajor-axis distribution if  $\langle e^2 \rangle^{1/2} \gtrsim 0.3$ .

On the other hand, the torques exerted by the gas ring strongly affect the orbital inclinations. In Figure 3 we show the inclination distribution at 3 Myr in each run, compared with the initial conditions. In the case of run A (Figure 3, top left panel), the inclination distribution of the stars changes significantly from the initial one, showing two peaks at  $\sim 27^\circ$  and  $50^\circ$  from

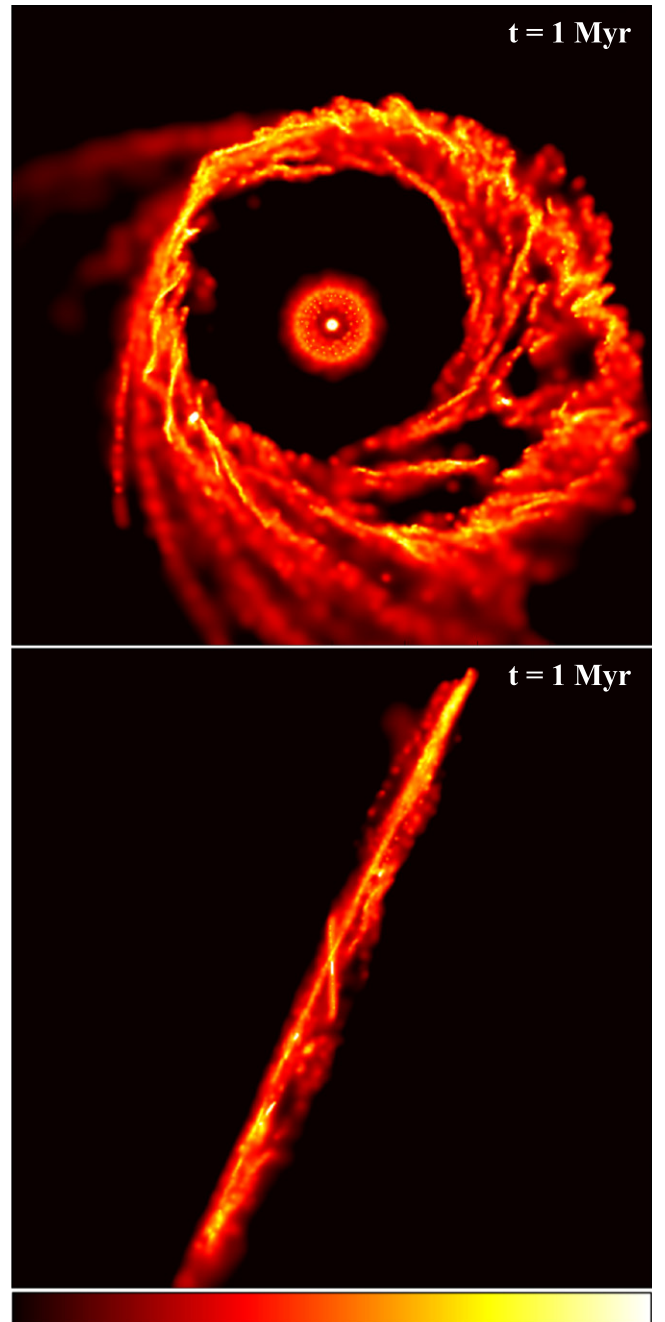


**Figure 1.** Color-coded maps of projected density of gas at 1 Myr in run A. Top panel: gas rings seen face-on. Bottom panel: gas rings seen edge-on. The inner gas ring is inclined by  $\sim 24^\circ$  with respect to the outer one. The top panel measures 8 pc per edge; the bottom panel measures 6 pc per edge. The color bar ranges from  $0.04$  to  $49 M_\odot \text{pc}^{-2}$  (from  $0.4$  to  $119 M_\odot \text{pc}^{-2}$ ).

the initial disk orientation. This indicates that the whole disk changed its orientation during the simulation.

In run B (Figure 3, top right panel), there is less spread in the inclinations than in run A and the inclination distribution at 3 Myr shows a main peak at  $\sim 42^\circ$ . As in run A, this means that the disk has completely changed its orientation with respect to the initial configuration. In run C the inclination distribution at 3 Myr is peaked at  $\sim 12^\circ$  and shows little spread.

In the case of run D (Figure 3, bottom right panel), the disk is unperturbed and the inclinations do not change as significantly

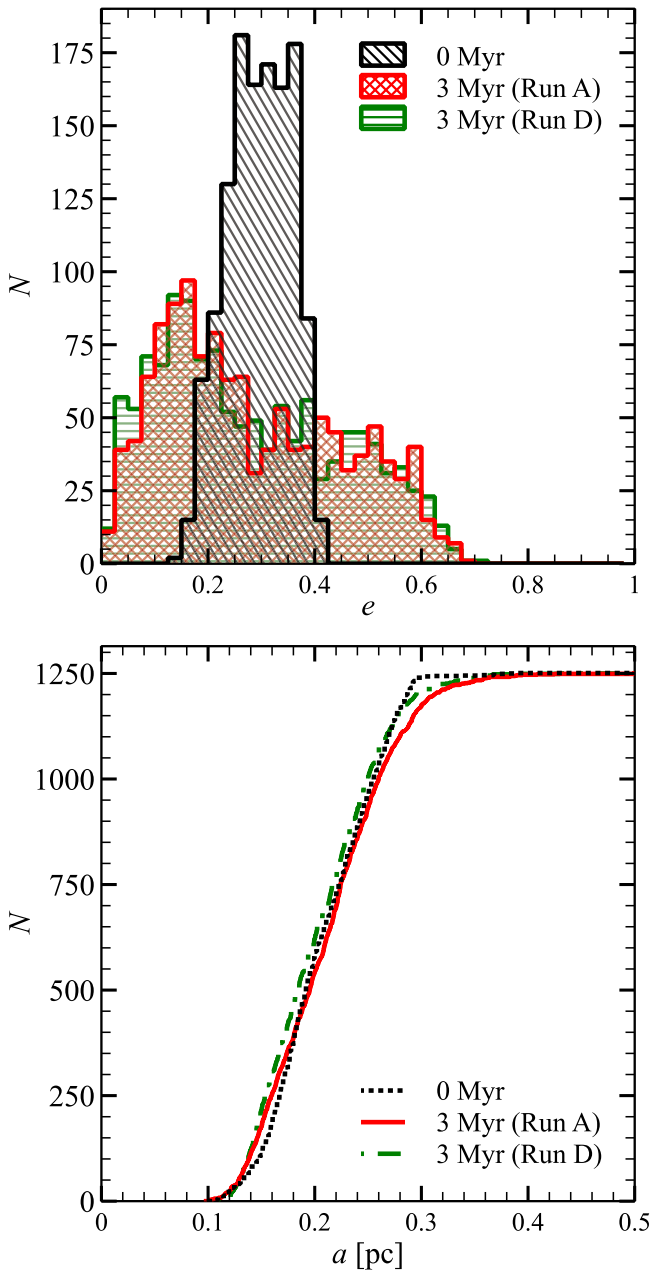


**Figure 2.** Top panel: eccentricity distribution of disk stars. Black hatched histogram: eccentricity distribution at the beginning of the integration. Red cross-hatched area: eccentricity distribution at 3 Myr in run A ( $\theta_i = 10^\circ$ ). Green horizontally hatched histogram: eccentricity distribution at 3 Myr in run D (no infalling gas cloud). Bottom panel: cumulative distribution of semimajor axis of disk stars. Black dotted line: distribution at the beginning of the integration. Red solid line: run A ( $\theta_i = 10^\circ$ ). Green dot-dashed line: run D (no infalling gas cloud).

as in the other runs. At 3 Myr the inclination distribution is broader than the initial one, but the disk has preserved its initial orientation.

In Figure 4 we show the evolution of the rms inclination  $\langle i^2 \rangle^{1/2}$  of the stars. In runs A, B, and C,  $\langle i^2 \rangle^{1/2}$  begins to increase after 0.75 Myr. In run A,  $\langle i^2 \rangle^{1/2}$  does not increase above  $35^\circ$ , while in run B it continues to increase. In run C the inclination increases more slowly, while in run D the evolution of  $\langle i^2 \rangle^{1/2}$  is negligible compared with the other runs.

The large spread in the inclination distribution of runs A and B indicates that the disk loses its coherence. In order to quantify the number of stars that are displaced from the disk, we define the disk membership criterion in a similar way to the one used by Haas et al. (2011a). In particular, we assume that a star belongs to the disk if its angular momentum deviates from the mean normalized angular momentum by less than  $20^\circ$ . We recompute the mean normalized angular momentum whenever a star is rejected as a disk member, until the number of disk members does not change anymore.

The number of disk members for different runs as a function of time is shown in Figure 5. While the number of disk members remains constant in runs C and D, in the other runs it begins to decrease after 0.75 Myr. In particular, the number of disk members decreases abruptly at  $\sim 1$  and  $\sim 1.25$  Myr in runs A and B, respectively. This abrupt change is a consequence of how disk membership is defined, indicating that most of the displaced stars cross the  $20^\circ$  threshold approximately at the same time. We find that at 3 Myr the number of disk members decreased by  $\approx 30\%$  and  $10\%$  in runs A and B, respectively.

Figure 6 shows the initial position of the stars, with the colors indicating the inclination of the star orbit at 3 Myr in run A. The color gradient indicates that the stars that are initially on outer orbits reach a higher inclination than the stars that are on inner orbits.

This trend is confirmed by Figure 7, which shows the average inclination as a function of the semimajor axis for runs A, B, and C at 3 Myr. In the initial disk, the inclinations are of  $\sim 7^\circ$  regardless of the semimajor axis. At 3 Myr, the average inclination has increased by  $30^\circ$ – $50^\circ$  depending on the run, and the individual inclinations have spread as shown by the error bars. Moreover, in runs A and B the average inclination is higher for larger semimajor axis. The origin of these differences between runs is discussed in the next section.

## 4. DISCUSSION

### 4.1. The Importance of the Inner Gas Ring

In our numerical model, the dynamics of the stellar disk are driven by two processes: two-body relaxation in the stellar disk and precession induced by the external potentials. The external potentials are the analytical cusp, which induces precession of the periastron and the gas ring. The gas ring is irregular and clumpy; however, we can consider its potential to be axisymmetric as a first approximation. Such axisymmetric potential induces precession of the mean orbital elements of a single star on a timescale given by the Kozai–Lidov timescale:

$$T_K = \frac{M_{\text{SMBH}}}{M_{\text{CNR}}} \frac{R_{\text{CNR}}^3}{\sqrt{GM_{\text{SMBH}}a^3}}, \quad (2)$$

where  $M_{\text{CNR}}$  and  $R_{\text{CNR}}$  are the mass and radius of the gas ring,  $G$  is the gravitational constant, and  $a$  is the semimajor axis of the star. The equations of motion of the mean orbital elements also depend on eccentricity  $e$  and argument of periastron  $\omega$  (e.g., see Šubr et al. 2009).

Since the gas ring is actually composed of two concentric rings, each component induces precession on the stellar disk on a different Kozai–Lidov timescale. The inner ring is less massive than the outer ring by a factor of  $\sim 30$  but has a  $\sim 5$  times smaller radius. Owing to the Kozai–Lidov timescale

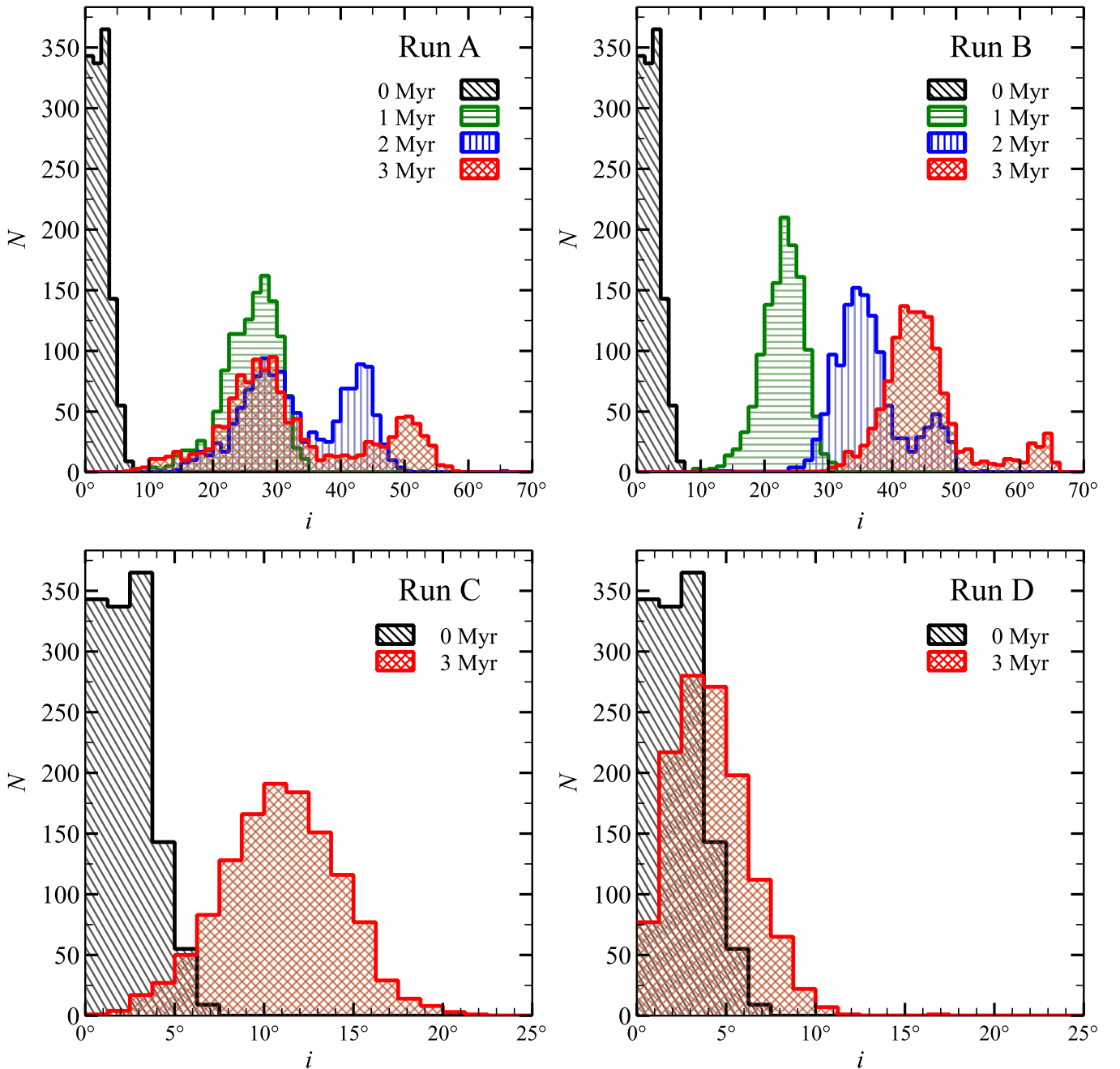


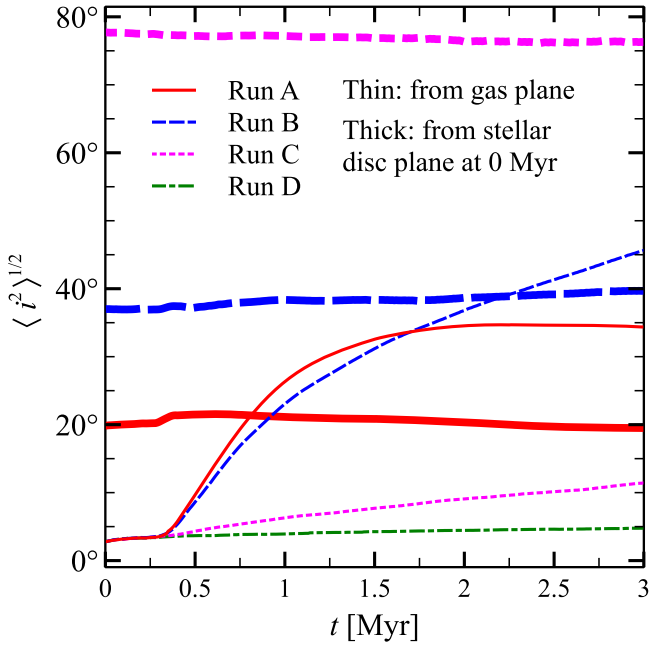
**Figure 3.** Distribution of the inclination of stellar orbits. From top left to bottom right: runs A, B, C, and D. In all panels, the black hatched histogram indicates the distribution at the beginning of the integration; the red cross-hatched histogram indicates the distribution at 3 Myr. In the top panels, the green horizontal-hatched histogram indicates the distribution at 1 Myr; the blue vertical-hatched area indicates the distribution at 2 Myr. In all panels, the inclination is measured with respect to the plane of the stellar disk at 0 Myr.

dependence  $T_K \propto M_{\text{CNR}}^{-1} R_{\text{CNR}}^3$ , the inner ring induces precession on a shorter timescale than the outer ring. We find  $T_K \sim 2$  Myr for the inner ring and  $T_K \sim 8$  Myr for the outer ring. Therefore, we expect that the precession of stars will be mainly driven by the inner ring rather than by the outer one.

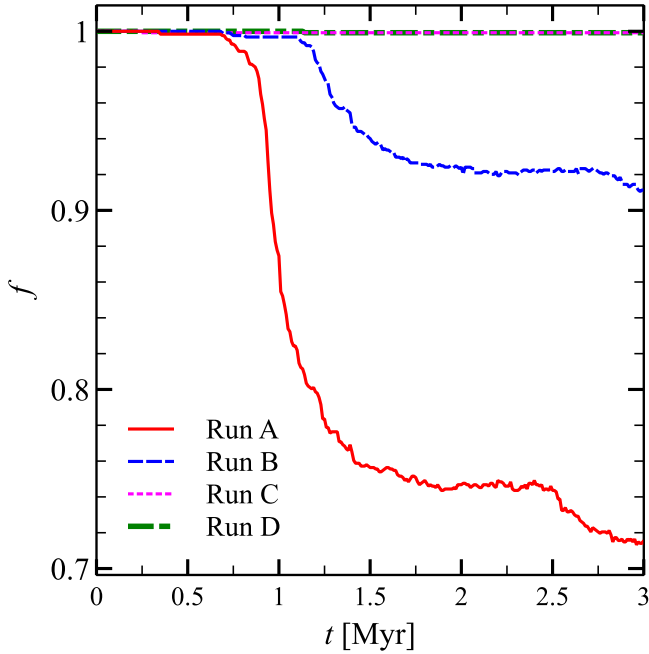
To check the importance of the outer ring, we run a simulation with the same initial conditions as run A but remove the gas particles with radius  $a > 0.9$  pc from the snapshots of the SPH simulation with  $t > 0.5$  Myr. In this way, we remove the outer ring from the simulation without affecting the evolution of the inner ring. In Figure 8 we compare the inclination distribution of this run, named A0, with that of run

A. The differences between the two runs are negligible; thus, the stellar disk is not affected by the outer gas ring and its evolution is driven mainly by the inner gas ring.

Figure 9 shows the time evolution of the density of normal vectors to the stellar orbits in run A. The normal vectors rotate about the angular momentum vector of the inner gas ring (marked with a green cross), losing coherence and forming a spiral-shaped tail. The normal vectors that form the spiral-shaped tail in Figure 9 correspond to the secondary peak at  $50^\circ$  in the top left panel of Figure 3. A similar spiral-shaped pattern was found by Löckmann et al. (2009), who simulated the interaction between two mutually inclined stellar disks (see



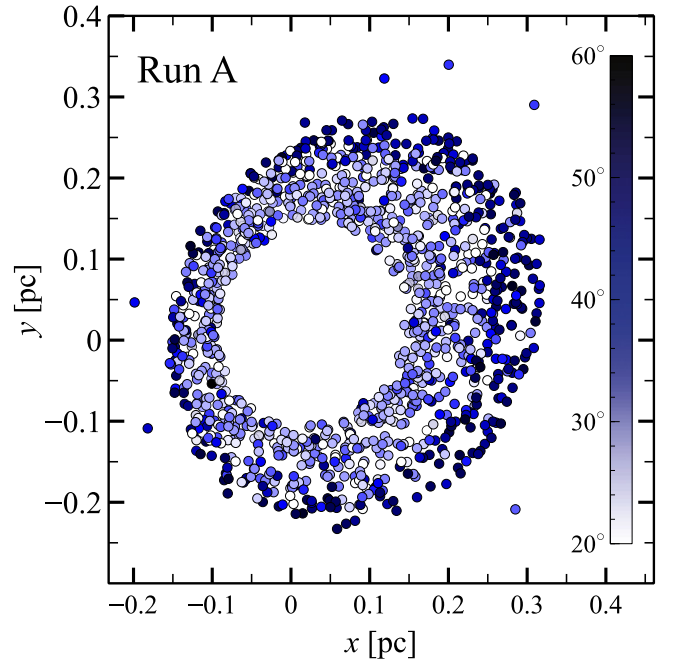
**Figure 4.** Root mean square inclination of the stellar disk as a function of time. Thin lines: inclination measured with respect to the plane of the stellar disk at 0 Myr. Thick lines: inclination measured with respect to the plane of the gas inner ring at 0.5 Myr. Red solid lines: run A ( $\theta_i = 10^\circ$ ). Blue dashed lines: run B ( $\theta_i = 45^\circ$ ). Magenta dotted lines: run C ( $\theta_i = 90^\circ$ ). Green dot-dashed line: run D (no infalling gas cloud).



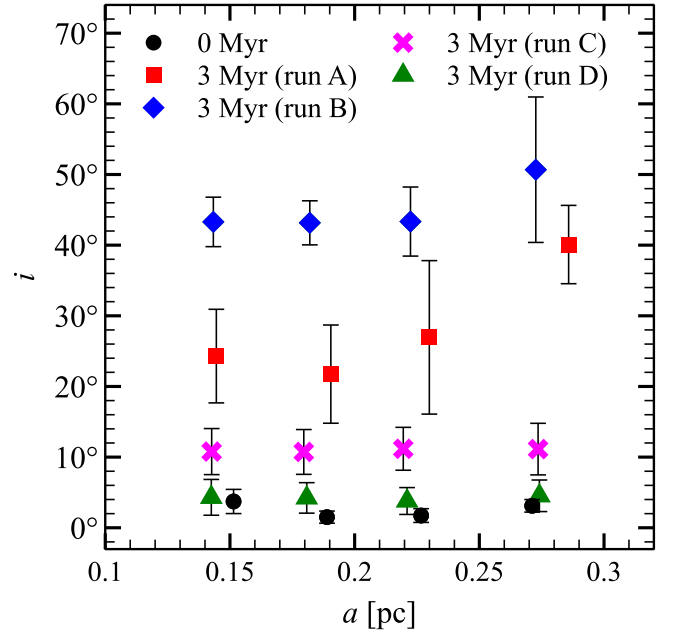
**Figure 5.** Fraction of stars with angular momentum deviating from the total angular momentum of the stellar disk by less than  $20^\circ$  as a function of time. Red solid line: run A ( $\theta_i = 10^\circ$ ). Blue dashed line: run B ( $\theta_i = 45^\circ$ ). Magenta dotted line: run C ( $\theta_i = 90^\circ$ ). Green dot-dashed line: run D (no infalling gas cloud). The magenta and green lines overlap.

Figure 2 of Löckmann et al. 2009). The formation of the tail is due to the combined effect of two-body relaxation and  $\Omega$  precession and will be discussed in Section 4.2.

In Section 3 (Figures 3–5) we showed that the inclination distribution changes faster in runs A and B than in run C. The reason for this is that the precession induced by an



**Figure 6.** Position of disk stars at 0 Myr, projected along the normal to the disk. The circles are colored according to the star inclinations at 3 Myr for run A ( $\theta_i = 10^\circ$ ). The inclinations are measured with respect to the normal to the stellar disk at 0 Myr and range from  $20^\circ$  to  $60^\circ$ .



**Figure 7.** Inclination as a function of the semimajor axis binned in four radial bins, so that each bin contains an equal number of stars. Black circles: inclination at  $t = 0$  Myr. Red squares: inclination at 3 Myr for run A ( $\theta_i = 10^\circ$ ). Blue diamonds: inclination at 3 Myr for run B ( $\theta_i = 45^\circ$ ). Magenta crosses: inclination at 3 Myr for run C ( $\theta_i = 90^\circ$ ). Green triangles: inclination at 3 Myr for run D (no infalling gas cloud). The inclination is measured with respect to the normal to the stellar disk at 0 Myr. Each point is the average inclination per bin, while the error bars show the standard deviation for each bin.

axisymmetric potential strongly depends on the angle between the individual stellar orbits and the gas ring. The timescale for precession of the longitude of the ascending node  $\Omega$  scales as  $\cos^{-1}\theta$ . In fact, in run C,  $\theta_{\text{inner}} \simeq 77^\circ$  and the  $\Omega$  precession is

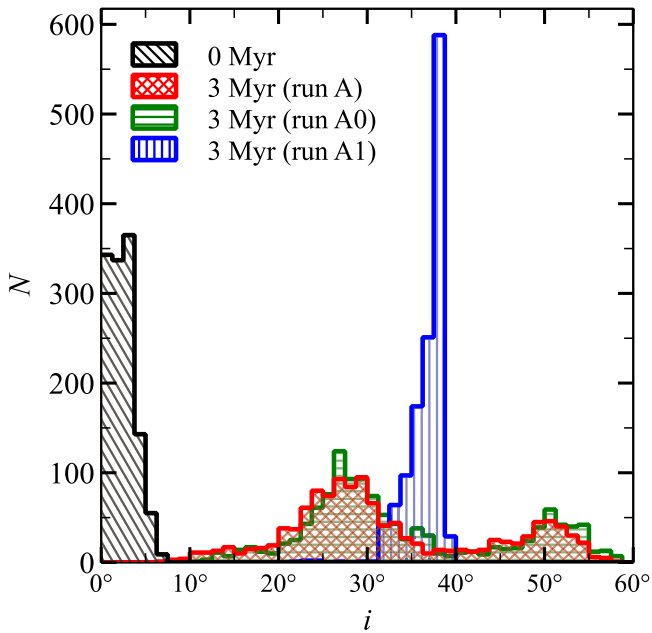


**Figure 8.** Inclination distribution of disk stars. Black hatched area: 0 Myr. Red cross-hatched area: run A at 3 Myr ( $\theta_i = 10^\circ$ ). Green horizontal-hatched area: run A0 at 3 Myr ( $\theta_i = 10^\circ$ , no outer gas ring). Blue vertical-hatched area: run A1 at 3 Myr ( $\theta_i = 10^\circ$ , massless stars). The inclination is measured with respect to the plane of the stellar disk at 0 Myr.

strongly suppressed. As a consequence, the rate of increase of stellar inclinations in run C is much smaller than in run A and B, while in run A ( $\theta_{\text{inner}} \simeq 22^\circ$ ) it is larger than in run B ( $\theta_{\text{inner}} \simeq 37^\circ$ ) (Figure 4).

However, the increase of stellar inclination in run A halts after 1.5 Myr. This is due to the fact that the changes in inclination are related to the changes in the longitude of the ascending node  $\Delta\Omega$ , which are limited in the range  $0-2\pi$ . The maximum inclination that can be achieved is  $i = 2\theta_{\text{inner}}$ , when  $\Delta\Omega = \pi$ . In run A  $\theta_{\text{inner}} \simeq 20^\circ$ , the inclination does not increase past  $i \simeq 40^\circ$ . After  $\Delta\Omega > \pi$  the inclination should decrease, while in run A it remains approximately constant. This can be due to the fact that these predictions hold in the approximation of a static, axisymmetric potential, while the inner gas ring in our simulations consists of particles that are gravitationally interacting. Two-body relaxation might also play a role in this.

The inner gas ring in our simulations has a density of  $10^6 \text{ cm}^{-3}$  and a temperature of 100–500 K, indicating that it is composed of warm, neutral gas. Jackson et al. (1993) estimated the presence of  $\gtrsim 300 M_\odot$  of dense neutral gas associated with the ionized gas within the cavity of the CNR. This estimate is one order of magnitude smaller than the mass of the inner ring in our simulations, but it is uncertain and only poses a lower limit to the amount of gas present since it does not account for ionized and molecular gas. More recent far-infrared observations suggest that shocks and/or photodissociation dominate the heating of hot molecular gas in the central cavity (Goicoechea et al. 2013). Therefore, a more accurate modeling of the central cavity would require a better treatment of ionization and radiative transfer. On the other hand, our results suggest that the kinematics of the CW disk (and of the other

young stars) can give us constraints on the gas mass in the central cavity.

#### 4.2. Two-body Relaxation

It has been demonstrated that the apsidal precession induced by the spherical cusp can suppress Kozai–Lidov oscillations (Chang 2009; Löckmann et al. 2009). In fact, we do not find evidences of Kozai–Lidov cycles in either inclination or eccentricity. Nonetheless, we find changes in the inclination and eccentricity distributions in our simulations (Figures 2, 3). The combined effect of two-body relaxation and eccentric disk instability accounts for changes in eccentricity.

The eccentricity becomes bimodal after 1.5 Myr (Figure 2, top panel). This is due to the eccentric disk instability described by Madigan et al. (2009), according to which the precession induced by a stellar cusp drives coherent torques that amplify deviations of individual orbital eccentricities from the average. In fact, we find the same bimodal distribution whether we include the gas ring. This result is in agreement with Gualandris et al. (2012), who find the same bimodal distribution evolving a similar stellar disk in the potential of a stellar cusp.

While eccentric disk instability accounts for the bimodality of the eccentricity distribution, two-body relaxation accounts for its overall evolution. According to the two-body relaxation theory of thin disks, the rms eccentricity and inclination should grow over time as (Stewart & Ida 2000; Šubr & Haas 2014)

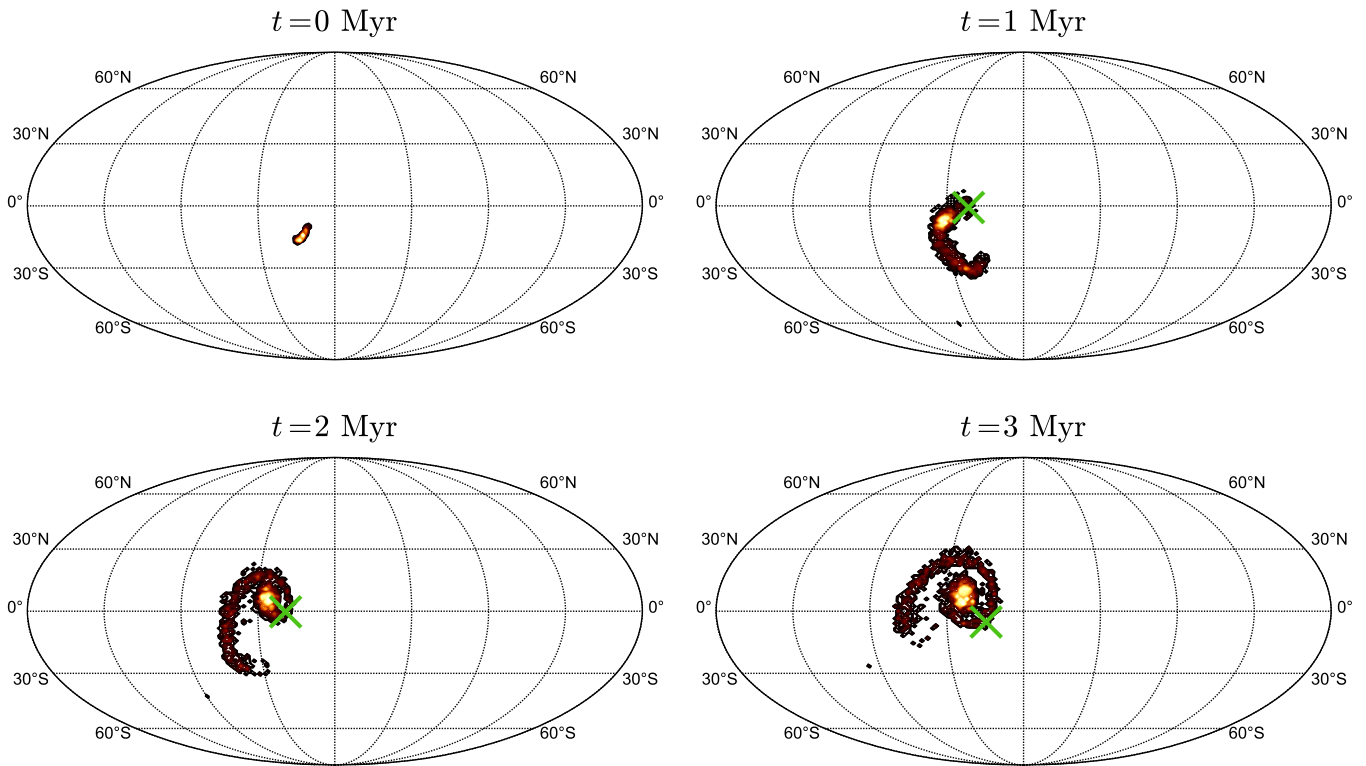
$$\langle i^2 \rangle^{1/2} \propto \langle e^2 \rangle^{1/2} \propto t^{1/4}. \quad (3)$$

Figure 10 shows the evolution of  $\langle e^2 \rangle^{1/2}$  and  $\langle i^2 \rangle^{1/2}$  along with the analytical predictions. It is apparent that the eccentricity evolution is well fit by the analytical predictions for both run A and D. This seems to indicate that the evolution of the eccentricity is predominantly driven by two-body relaxation.

This is not the case for the evolution of inclinations. While the rms inclination of run D is consistent with the analytical predictions of two-body relaxation, the fit is inconsistent for runs A, B, and C. This is due to torques exerted by the gas ring onto the stellar disk. In fact, while the spherical cusp suppresses Kozai–Lidov cycles, it does not hinder the precession of the longitude of the ascending node as measured in the reference frame of the gas ring (Šubr et al. 2009). Such precession appears as a change in inclination in the reference frame of the stellar disk. This effect is apparent in Figure 4, which shows that the rms inclination of the stars remains constant if measured from the plane of the inner gas ring.

Moreover, runs A, B, and C show higher inclinations at larger radius (Figure 7). This is due to the fact that the stars on the outer orbits precess faster than those in the inner ones, as expected from the dependence of precession timescale on the semimajor axis ( $T_K \propto a^{-3/2}$ , Equation (2)). This is in agreement with Mapelli et al. (2013).

Since the stars of the disk have different eccentricity and semimajor axis, they precess at different rates, ultimately causing the disk to dismember. The diffusion of the orbital parameters due to two-body relaxation enhances differential precession, accelerating the dismembering of the disk. To test the importance of two-body relaxation, we run a simulation (named A1) with the same initial conditions as run A except that we set the stellar masses to zero. In this way we inhibit



**Figure 9.** Density of normal vectors to the stellar orbits at different times for run A. From top left to bottom right:  $t = 0, 1, 2,$  and  $3$  Myr. The green cross indicates the total angular momentum vector of the inner gas ring (not yet formed at  $t = 0$  Myr). Projected using the Mollweide projection.

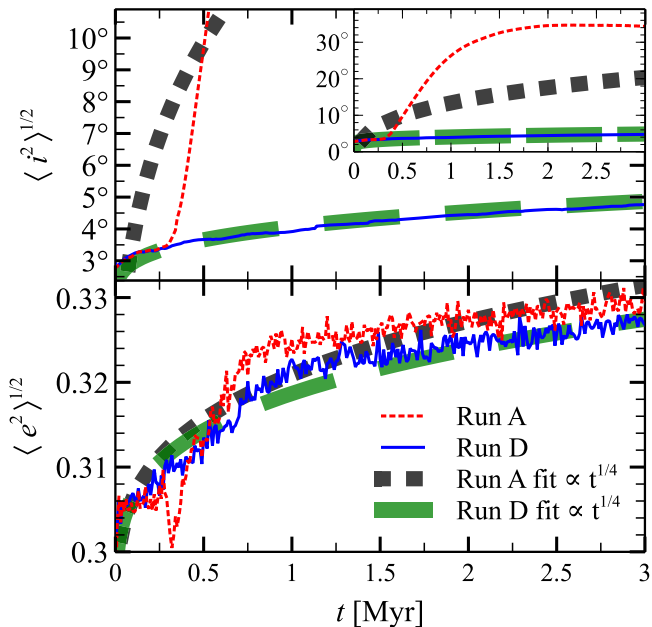


**Figure 10.** Root mean squared inclination (top) and eccentricity (bottom) as a function of time. Thin blue solid line: rms values for run D (no infalling gas cloud). Thin red dotted line: rms values for run A ( $\theta_i = 10^\circ$ ). The thick lines are fit functions  $\propto t^{1/4}$ ; dashed green lines for run D and dotted black lines for run A. Inset: same as the top panel, but zoomed out to  $40^\circ$ .

two-body relaxation, and the evolution of stellar orbits is driven by the external potentials.

The inclination distribution in run A1 at 3 Myr is shown in Figure 8. In contrast to run A, the inclinations do not spread and the distribution does not become bimodal. This indicates that the disk changes its orientation without losing coherence

and the spiral-shaped tail of normal vectors in Figure 9 does not form. Thus, two-body relaxation is a key process in understanding the dismembering of a nearly Keplerian disk. This result is in agreement with the findings of Haas et al. (2011a).

Because the stellar cusp is modeled as a rigid potential, we neglect additional two-body relaxation between cusp and disk stars. Löckmann & Baumgardt (2009) showed that a cusp of stellar remnants enhances the relaxation of angular momentum, which increases orbital eccentricities and disk thickness (Löckmann et al. 2009). However, Löckmann & Baumgardt (2009) find that the relaxation among disk stars dominates over the relaxation between cusp and disk stars. Thus, we expect that a grainy cusp would enhance the disk disruption in our simulations by a negligible amount.

## 5. CONCLUSIONS

We investigate the effect of gas rings on a nearly Keplerian stellar disk orbiting an SMBH by means of combined SPH and direct  $N$ -body simulations. We simulate the formation of a CNR-like gas ring through the infall and disruption of a molecular gas cloud toward the SMBH. In particular, the gas cloud settles down into two concentric rings around the SMBH: the outer ring matches the properties of the CNR in the GC (inner radius  $R_{\text{CNR}} \sim 1.5$  pc, mass  $M_{\text{CNR}} \sim 10^4 M_\odot$ ), while the inner ring is less massive ( $\sim 10^3 M_\odot$ ) and has an outer radius of  $\sim 0.4$  pc.

We use the AMUSE software to couple the SPH simulation of the infalling gas cloud to a direct  $N$ -body code, which we use to integrate the evolution of the stellar disk. The stellar disk has properties similar to the CW disk and was formed self-consistently by the infall and collapse of a disrupted molecular cloud. Our simulations include the effect of the stellar cusp,



modeled as a rigid potential. We simulate different inclinations  $\theta_i$  between the infalling gas cloud and the stellar disk:  $\theta_i = 10^\circ$  (run A),  $45^\circ$  (run B), and  $90^\circ$  (run C).

We find that the outer ring is inefficient in affecting the stellar orbits on a timescale of 3 Myr. On the other hand, the inner ring of gas can significantly affect the stellar disk inclination and coherence.

The inner gas ring induces precession of the longitude of the ascending node  $\Omega$  on the disk stars, which appears as a change of the inclinations in the reference frame of the stellar disk. As a consequence, the disk precesses about the axis of symmetry of the inner gas ring. We do not find precession of eccentricity and inclination with respect to the gas ring because it is suppressed by the stellar cusp.

We find that the precession of  $\Omega$  is faster for smaller angles between the stellar disk and the inner gas ring  $\theta_{\text{inner}}$ , as expected from timescale dependence  $T_K \propto \cos^{-1}(\theta_{\text{inner}})$ . After 3 Myr, the stellar disk has changed its orientation by  $35^\circ$ ,  $45^\circ$ , and  $10^\circ$  in runs A ( $\theta_{\text{inner}} \simeq 20^\circ$ ), B ( $\theta_{\text{inner}} \simeq 37^\circ$ ), and C ( $\theta_{\text{inner}} \simeq 77^\circ$ ), respectively. Since the inclination changes are driven by  $\Omega$ -precession, the stellar disk inclination cannot increase more than twice the angle between the gas ring and the stellar disk; as a consequence, the stars in run B achieve a higher inclination with respect to run A.

We find that the combined effect of two-body relaxation and  $\Omega$ -precession can displace stars from the disk. We verified that neither process can drive the disk dismembering alone. Two-body relaxation introduces a spread in the orbital elements of the individual stars of the disk, inducing differential precession. This differential precession leads to the dismembering of the stellar disk, which loses 30% of the stars in run A ( $\theta_{\text{inner}} \simeq 20^\circ$ ) at 3 Myr. In run B ( $\theta_{\text{inner}} \simeq 37^\circ$ ), the disk lost only 10% of the stars in 3 Myr, while in run C ( $\theta_{\text{inner}} \simeq 77^\circ$ )  $\Omega$ -precession is inefficient and the stellar disk remains coherent.

In conclusion, our simulations show that the gas in the innermost 0.5 pc (i.e., the inner cavity) can play a crucial role in the evolution of the stellar orbits in the GC.

We thank the anonymous referee for his/her invaluable comments. We thank Alessia Gualandris, Mario Spera, Brunetto Marco Ziosi, Edwin van der Helm, Bence Kocsis, and Lucie Jílková for useful discussions.

A.A.T., M.M., and A.B. acknowledge financial support from INAF through grant PRIN-2014-14. M.M. acknowledges financial support from the Italian Ministry of Education, University and Research (MIUR), through grant FIRB 2012 RBF12PM1F and from Fondation MERAC through grant ‘‘The physics of gas and protoplanetary discs in the Galactic centre.’’ This work was supported by the Interuniversity Attraction Poles Programme initiated by the Belgian Science Policy Office (IAP P7/08CHARM) and by the Netherlands Research Council NWO (grants #643.200.503, #639.073.803 and #614.061.608) and by the Netherlands Research School for Astronomy (NOVA).

## REFERENCES

- Alig, C., Burkert, A., Johansson, P. H., & Schartmann, M. 2011, *MNRAS*, 412, 469
- Alig, C., Schartmann, M., Burkert, A., & Dolag, K. 2013, *ApJ*, 771, 119
- Bartko, H., Martins, F., Fritz, T. K., et al. 2009, *ApJ*, 697, 174
- Bédorf, J., Gaburov, E., & Portegies Zwart, S. 2015, *ComAC*, 2, 8
- Bonnell, I. A., & Rice, W. K. M. 2008, *Sci*, 321, 1060
- Chang, P. 2009, *MNRAS*, 393, 224
- Dehnen, W., & Read, J. I. 2011, *EPJP*, 126, 55
- Do, T., Lu, J. R., Ghez, A. M., et al. 2013, *ApJ*, 764, 154
- Eisenhauer, F., Genzel, R., Alexander, T., et al. 2005, *ApJ*, 628, 246
- Fujii, M., Iwasawa, M., Funato, Y., & Makino, J. 2007, *PASJ*, 59, 1095
- Gaburov, E., Harfst, S., & Portegies Zwart, S. 2009, *NewA*, 14, 630
- Genzel, R., Schödel, R., Ott, T., et al. 2003, *ApJ*, 594, 812
- Ghez, A. M., Duchêne, G., Matthews, K., et al. 2003, *ApJL*, 586, L127
- Ghez, A. M., Hornstein, S. D., Lu, J. R., et al. 2005, *ApJ*, 635, 1087
- Gillessen, S., Eisenhauer, F., Trippe, S., et al. 2009, *ApJ*, 692, 1075
- Goicoechea, J. R., Etxaluze, M., Cernicharo, J., et al. 2013, *ApJL*, 769, L13
- Gualandris, A., Mapelli, M., & Perets, H. B. 2012, *MNRAS*, 427, 1793
- Haas, J., Šubr, L., & Kroupa, P. 2011a, *MNRAS*, 412, 1905
- Haas, J., Šubr, L., & Vokrouhliký, D. 2011b, *MNRAS*, 416, 1023
- Harfst, S., Gualandris, A., Merritt, D., et al. 2007, *NewA*, 12, 357
- Hayfield, T., Mayer, L., Wadsley, J., & Boley, A. C. 2011, *MNRAS*, 417, 1839
- Hobbs, A., & Nayakshin, S. 2009, *MNRAS*, 394, 19
- Ivanov, P. B., Polnarev, A. G., & Saha, P. 2005, *MNRAS*, 358, 1361
- Jackson, J. M., Geis, N., Genzel, R., et al. 1993, *ApJ*, 402, 173
- Jalali, B., Pelupessy, F. I., Eckart, A., et al. 2014, *MNRAS*, 444, 1205
- Kozai, Y. 1962, *AJ*, 67, 591
- Krabbe, A., Genzel, R., Drapatz, S., & Rotaciuc, V. 1991, *ApJL*, 382, L19
- Krabbe, A., Genzel, R., Eckart, A., et al. 1995, *ApJL*, 447, L95
- Lidov, M. L. 1962, *P&SS*, 9, 719
- Löckmann, U., & Baumgardt, H. 2009, *MNRAS*, 394, 1841
- Löckmann, U., Baumgardt, H., & Kroupa, P. 2009, *MNRAS*, 398, 429
- Lu, J. R., Do, T., Ghez, A. M., et al. 2013, *ApJ*, 764, 155
- Lu, J. R., Ghez, A. M., Hornstein, S. D., et al. 2009, *ApJ*, 690, 1463
- Lucas, W. E., Bonnell, I. A., Davies, M. B., & Rice, W. K. M. 2013, *MNRAS*, 433, 353
- Madigan, A.-M., Levin, Y., & Hopman, C. 2009, *ApJL*, 697, L44
- Mapelli, M., & Gualandris, A. 2016, in *Astrophysical Black Holes*, ed. F. Haardt et al. (Berlin: Springer), 205
- Mapelli, M., Gualandris, A., & Hayfield, T. 2013, *MNRAS*, 436, 3809
- Mapelli, M., Hayfield, T., Mayer, L., & Wadsley, J. 2008, arXiv:0805.0185
- Mapelli, M., Hayfield, T., Mayer, L., & Wadsley, J. 2012, *ApJ*, 749, 168
- Mapelli, M., & Ripamonti, E. 2015, *ApJ*, 806, 197
- Mapelli, M., & Trani, A. A. 2015, *A&A*, 585, 161
- Morris, M. 1993, *ApJ*, 408, 496
- Paumard, T., Genzel, R., Martins, F., et al. 2006, *ApJ*, 643, 1011
- Pelupessy, F. I., van Elteren, A., de Vries, N., et al. 2013, *A&A*, 557, A84
- Portegies Zwart, S., McMillan, S., Harfst, S., et al. 2009, *NewA*, 14, 369
- Portegies Zwart, S., McMillan, S. L. W., van Elteren, E., Pelupessy, I., & de Vries, N. 2013, *CoPhC*, 183, 456
- Read, J. I., Hayfield, T., & Agertz, O. 2010, *MNRAS*, 405, 1513
- Schödel, R., Eckart, A., Alexander, T., et al. 2007, *A&A*, 469, 125
- Schödel, R., Ott, T., Genzel, R., et al. 2003, *ApJ*, 596, 1015
- Stewart, G. R., & Ida, S. 2000, *Icar*, 143, 28
- Šubr, L., & Haas, J. 2012, *JPhCS*, 372, 012018
- Šubr, L., & Haas, J. 2014, *ApJ*, 786, 121
- Šubr, L., Schovancová, J., & Kroupa, P. 2009, *A&A*, 496, 695
- Ulubay-Siddiki, A., Gerhard, O., & Arnaboldi, M. 2009, *MNRAS*, 398, 535
- Wadsley, J. W., Stadel, J., & Quinn, T. 2004, *NewA*, 9, 137
- Wisdom, J., & Holman, M. 1991, *AJ*, 102, 1528
- Yelda, S., Ghez, A. M., Lu, J. R., et al. 2014, *ApJ*, 783, 131
- Zemp, M., Stadel, J., Moore, B., & Carollo, C. M. 2007, *MNRAS*, 376, 273